Band-bending induced passivation: high performance and stability perovskite solar cells using perhydropoly(silazane) precursor

Hiroyuki Kanda[1], Naoyuki Shibayama[2], Aron Joel Huckaba[1], Yonghui Lee[1],

Sanghyun Paek[1], Nadja Klipfel[1], Cristina Roldán Carmona[1], Valentin Ianis Emmanuel Queloz[1],

Giulia Grancini[1], Yi Zhang[1], Mousa Abuhelaiqa[1], Kyung Taek Cho[1],

Mo Li[3,4], Mounir Driss Mensi[1], Sachin Kinge,[5] and Mohammad Khaja Nazeeruddin[1*]

Corresponding author: mdkhaja.nazeeruddin@epfl.ch (Mohammad Khaja Nazeeruddin)

[1]Group for Molecular Engineering of Functional Materials, École Polytechnique Fédérale de Lausanne, Valais Wallis, CH-1951 Sion, Switzerland.

[2]Department of General Systems Studies, Graduate School of Arts and Sciences, The University of Tokyo, 3-8-1 Komaba, Meguro-ku, Tokyo 153-8902, Japan.

[3]Laboratory of Materials for Renewable Energy, École Polytechnique Fédérale de Lausanne, Valais Wallis, CH-1951 Sion, Switzerland.

[4]Swiss Federal Laboratories for Materials Science and Technology, CH-8600 Dübendorf, Switzerland

[5]Toyota Motor Corporation, Toyota Motor Technical Centre, Advanced Technology Div., Hoge Wei 33, B-1930 Zaventum, Belgium.

Keywords: perovskite, solar cell, passivation, perhydropolysilazane, silicon oxide, Fermi-level of the perovskite.

Abstract

Surface passivation of the perovskite photo absorber is a key factor to improve photovoltaic performance. So far robust passivation strategies have not yet been revealed. Here, we demonstrate a successful passivation strategy which controls the Fermi-level of the perovskite surface by improving surface states. Such Fermi-level control caused a band-bending between the surface and bulk of the perovskite, which enhanced the hole-extraction from the absorber bulk to the HTM side. As an added benefit, inorganic passivation layer improved the device stability, as well as remarkable waterproof protection. As a result, an enhancement of V_{OC} and conversion efficiency from 20.5% to 22.1% was achieved. We revealed these passivation mechanisms and used perhydropoly(silazane) (PHPS) derived silica to control the perovskite surface state.

Introduction

Since the first report of the hybrid inorganic-organic perovskite solar cell[1-4], a new epoch of solar cell research dawned[5-9], resulting in device efficiencies of 24.2%[10]. Metal halide perovskite semiconductors have several significant characteristics of optoelectronic properties, such as large absorption coefficient[11,12], long charge carrier diffusion length[13-16], and easily tunable bandgap[17-19]. These unique semiconductor characteristics could allow efficiency values to approach the Shockley–Queisser limit[20-22]. To further improve the photovoltaic performance beyond the current state of the art, passivation strategies are still needed.

To yield surface passivation in perovskite solar cells, passivation materials such as poly(methyl methacrylate) (PMMA)[23], polyvinylpyrrolidone (PVP)[24,25], phenylethylammonium iodide (PEAI)[26], n-hexyl trimethyl ammonium bromide (HTAB)[27], and choline chloride[28-30] have been used. However, it is still not thoroughly investigated why the passivation layer improves the carrier dynamics in perovskite devices. Thus, a more in-depth understanding of passivation design strategy needs to be gained to improve further perovskite solar cell efficiencies.

Band-bending is the shifting of energy band structure caused by difference of the fermi level. The main principle underlying the band bending inside the semi-conductor is the local imbalance space charge[31]. Such band-bending could influence the carrier dynamics at semiconductor surface[32-35]. Therefore, passivation induced by the band-bending can expect to reduce carrier recombination.

In this study, we demonstrate that the band-bending induced passivation can have a beneficial effect on the photovoltaic performance of perovskite solar cells. The influence of the passivation layer on the band structure

was investigated by varying precursor concentration, herewith, we propose the novel passivation concept as band-bending passivation. As an added benefit, inorganic passivation layer improved the device stability, and remarkable waterproof protection. The experimental results provide a way towards the implementation of a passivation design strategy for perovskite solar cells.

Material characteristics

Perhydropoly(silazane) (PHPS) is a saturated inorganic polymer consisting of alternating nitrogen-silicon bonds, see Fig. 1a. The reaction of PHPS with oxygen or water generates amorphous silicon dioxide at room temperature (Fig. 1b). The amino groups of PHPS interact with the perovskite surface, which affects the energy band structure on the surface of the perovskite layer. Therefore, it is expected to function as an inorganic passivation layer having a function on surface modification perovskite.

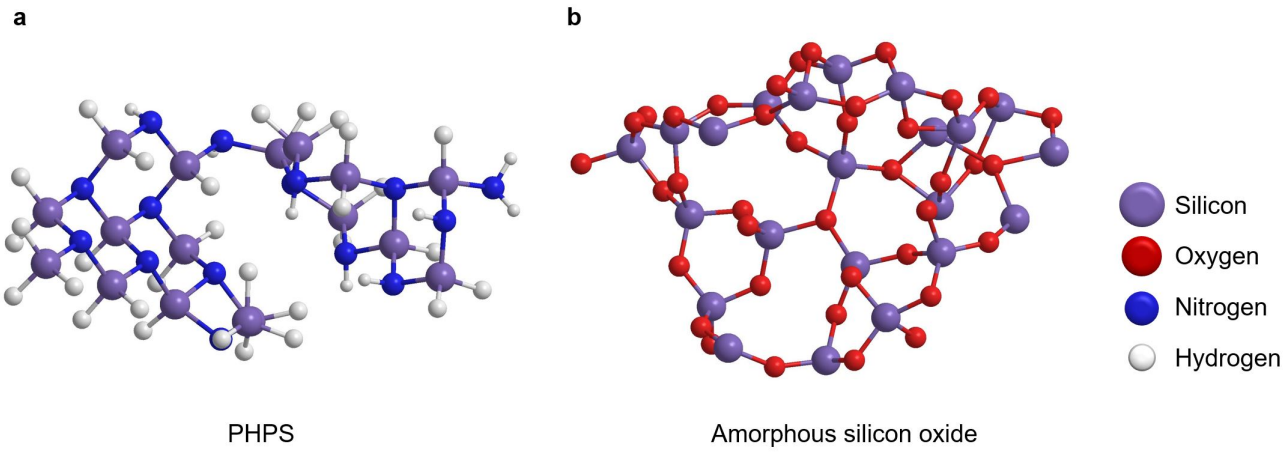

Fig. 1 Representative chemical structures: a, Perhydropoly(silazane) (PHPS). **b**, Amorphous silicon oxide.

To confirm the presence of the PHPS-derived passivation materials, XPS measurements were performed (Fig. 2). After depositing PHPS on a perovskite film, the binding energies of the characteristic Si 2p, O 1s, and N 1s peaks were measured. The PHPS solution concentration was varied in the range of 0.01—0.2 vol.%, and a perovskite sample without PHPS deposition was also analyzed under the same conditions as a reference. In the Si 2p spectra (Fig. 2a), the peak intensity of Si 2p increased with the increasing PHPS concentration. The

observed Si 2p signal (Fig. 2a) consists of two contributions, which were identified as Si^{4+} (103.3 eV) and Si-O-N (102.5 eV), respectively[36,37]. At low concentration (0.01 vol.%), the component of Si^{4+} peak was predominant, while the proportion of the Si-O-N component increased with increasing PHPS concentration. In the O 1s spectra (Fig. 2b), a peak was identified as Si-O bond (532.8 eV). We reasoned that PHPS oxidation in ambient air led to Si-O bond formation. In the N 1s spectrum (Fig. 2c), signals corresponding to N-C (400.2 eV) and Si-O-N (398.4 eV) were correlated to perovskite and silicon oxynitride, respectively[37]. These results confirmed the presence of a PHPS derived material on the perovskite surface, which was identified as silicon oxide and silicon oxynitride, forming a thin layer not detectable by the cross-sectional SEM image (Supplementary Fig. 1). Furthermore, at low PHPS concentration, we could only detect silicon dioxide while using higher PHPS concentrations yielded silicon dioxide/silicon oxynitride composites, probably due to the incomplete reaction of the PHPS precursor. It is worth to note here that we also observed an apparent effect on the perovskite signals after depositing the passivate (Supplementary Fig. 2). As observed in the Figure, a clear shift in the Pb 4f binding energy takes place with increasing the silicon oxide signal (Si-O), while a shift in the I 3d peak occurs simultaneously with the appearance of silicon oxynitride peak (Si-O-N). These results suggest a strong change on the electronic state around the perovskite surface atoms, which can be due to the interaction of Pb/SiOx or I/SiON, respectively.

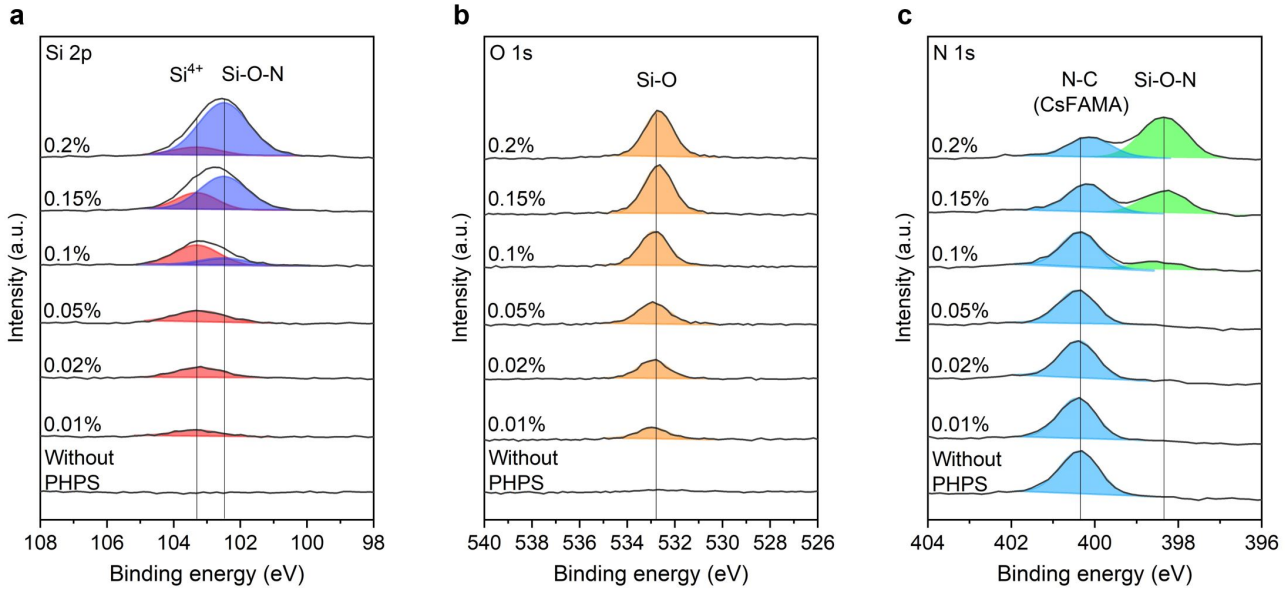

Fig. 2 Material characteristics for passivation layer. a-c, XPS spectra and fitting results of passivation materials on the perovskite layer of Si 2p (a), O 1s (b), and N 1s (c) as a function of PHPS concentration.

To determine if the passivation layer affected the perovskite crystallinity and crystallite orientation, we analyzed the perovskite with and without PHPS treatment by Two-dimensional Wide-Angle X-Ray Scattering (2D-WAXS) (Fig. 3). The reciprocal lattice mapping data indicated random crystallite orientation for samples with and without passivation layer as shown in Fig. 3a and b, respectively. Both perovskite layers exhibited an identical cubic structure, which was confirmed through analyzing the integrated intensity profiles of the 2D-WAXS at 100, 110, 111, 200, and 211 reflections (Fig. 3c)[38-40]. It could, therefore, be confirmed that the passivation layer did not affect the perovskite crystal orientation and structure. Furthermore, no silicon oxide reflection was observed, probably due to an amorphous state of the material.

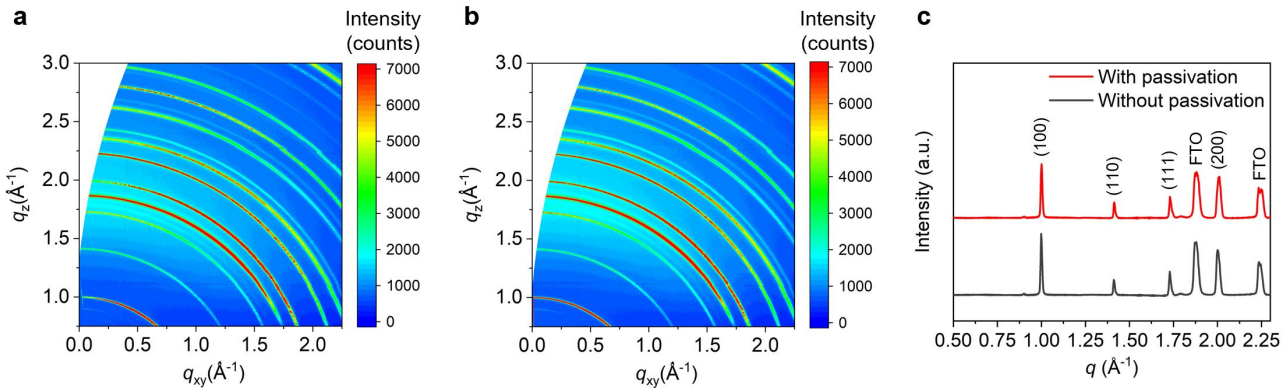

Fig. 3 Crystallinity of the perovskite layer with and without passivation. a,b, 2D-WAXS patterns of perovskite layer with (a) and without (b) passivation. **c,** Integrated intensity profiles from 2D-WAXS data with and without passivation. (PHPS concertation is 0.02 vol.%.)

Photovoltaic performance

We further investigated the influence of the passivation layer on the device efficiency (Fig. 4). Fig. 4a shows the *I-V* curve for the champion cell with passivation compared to the reference sample without passivation process. By applying the passivation layer, the V_{OC} was increased from 1.052 V up to 1.135 V (Fig. 4a), which lead to a photoconversion efficiency of 22.13% and superior photovoltaic properties (Supplementary Fig. 3-4). The high efficiency of 21.73% certified data is shown in Supplementary Fig. 5. The Fig. 4b shows V_{OC} distribution as a function of the PHPS concentration. The average V_{OC} value was increased to 1.117 V from 1.061 V without PHPS passivation when depositing a 0.02 vol.% solution of PHPS. With increasing PHPS concentration (from 0.01 to 0.2%), the average V_{OC} increased up to 1.135 V for 0.2 vol.% PHPS. Overall, these results confirm the beneficial effect of PHPS-derived passivation on the V_{OC}, and call for deeper investigations.

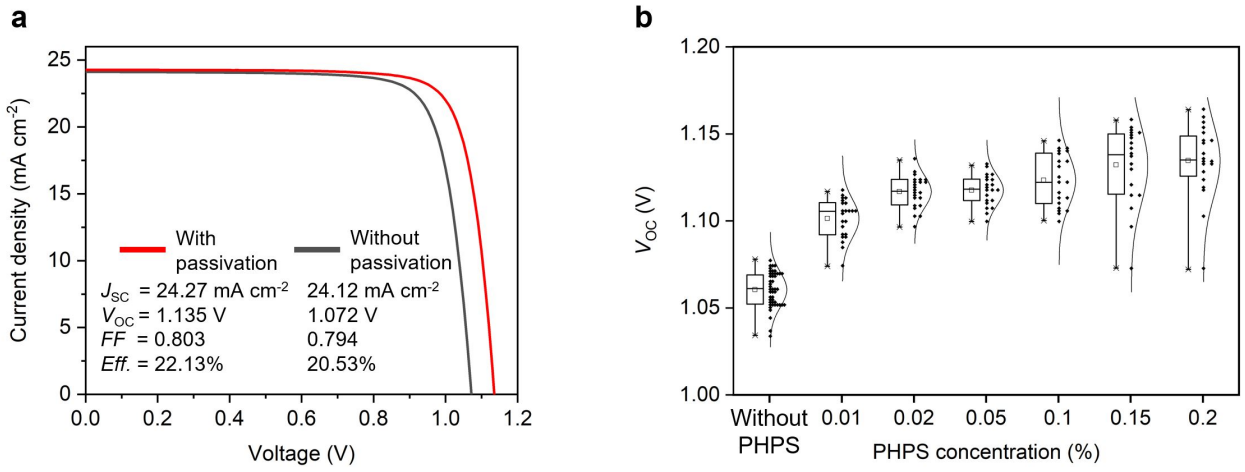

Fig. 4 Photovoltaic performance. a, *I-V* curves and photovoltaic properties of best perovskite solar cell with (PHPS concentration 0.02 vol%) and without passivation. **b,** V_{OC} distribution as a function of PHPS concentration.

To understand more in detail why the V_{OC} was improved, steady-state PL spectra and PL decay measurements were performed at varied PHPS concentration. Results obtained for Glass/Perovskite/Passivation layer samples with varying PHPS concentration are shown in Fig. 5a and Supplementary Fig. 6 respectively. Note that the perovskite thickness is the same for all the samples. The intensity of the observed emission peak close to 800 nm increased with increasing PHPS concentration on the perovskite layer compared to the reference sample without passivation, which suggests that the passivation layer reduces the nonradiative pathways. This is in consistence with the enhanced emission lifetime shown in Supplementary Fig. 6 and in correspondence with what has been reported before for passivation with PMMA, PVP, PEAI, and choline chloride[23,24,26,28].

Glass/Perovskite/Passivation layer/Spiro-OMeTAD samples were also prepared to elucidate the hole-transportation at Perovskite/Passivation layer/HTM interface (Fig. 5b, Supplementary Fig. 7). For concentrations up to 0.1%, the PL dynamics are increased when comparing to the reference sample, indicating that upon the addition of the passivation layer a new decay channel is opened. This can be related to hole transfer enhancement from the perovskite to the HTM through the passivation layer. For concentrations beyond 0.1%, however, the dynamics are slowed down possibly indicating that the hole transfer is prevented due to the enhanced thickness of the passivation layer. Indeed, as Wolff et al.,[41] have demonstrated, upon inserting an inert interfacial layer, the PL decay is slowed down due to reduced back electron-hole recombination. This phenomenon could explain our observations in the PL decay for PHPS > 0.1%. To verify this possibility, we measured the series resistance as a function of PHPS concentration. We found that the series resistance increases up to 45 Ω (at 0.2 vol.%) from 10 Ω (at 0.02 vol.%), as well as *FF* decrease to 0.738 (at 0.2 vol.%) from 0.799

(at 0.02 vol.%). This indicates that hole transfer is hampered at increased PHPS concentration. Also, the perovskite solar cell ideality factor improved to 1.58 with passivation from 1.64 without passivation (PHPS=0.02 vol.%) (Supplementary Fig. 8)[42], suggesting that PHPS passivation reduces Shockley-Read Hall recombination.

To further investigate the origin of the improved hole-extraction, the energy band diagram with and without passivation was analyzed by ultraviolet photoelectron spectroscopy (UPS) and angle-resolved hard X-ray photoelectron spectroscopy[43-45] (AR-HAXPES) (Fig. 5c). After passivation (PHPS=0.02 vol.%), the Fermi-level of the perovskite surface was shifted to –4.68 eV from –4.56 eV as indicated in Supplementary Fig. 9,10. Interestingly, we revealed that the Fermi level of the perovskite was gradually shifted to the intrinsic-side with approaching to the surface from the bulk (Fig. 5d, Supplementary Fig. 11). This Fermi-level shift can be due to the interaction of the lead with the silica passivation. Also, it was confirmed the that the passivation treatment affect on only the perovskite surface because the 2D WAXS shows the inside of the perovskite (Fig. 3), which is consistent with AR-HAXPES result. In other words, in the case of samples with passivation, there was a noticeable difference between the surface and bulk Fermi-levels. Such Fermi-level differences can cause band-bending, which is a driving force for the hole-extraction to the HTM (Fig. 5e). Therefore, PHPS derived passivation layer could serve to increase the V_{OC} and photoconversion efficiency in perovskite solar cells.

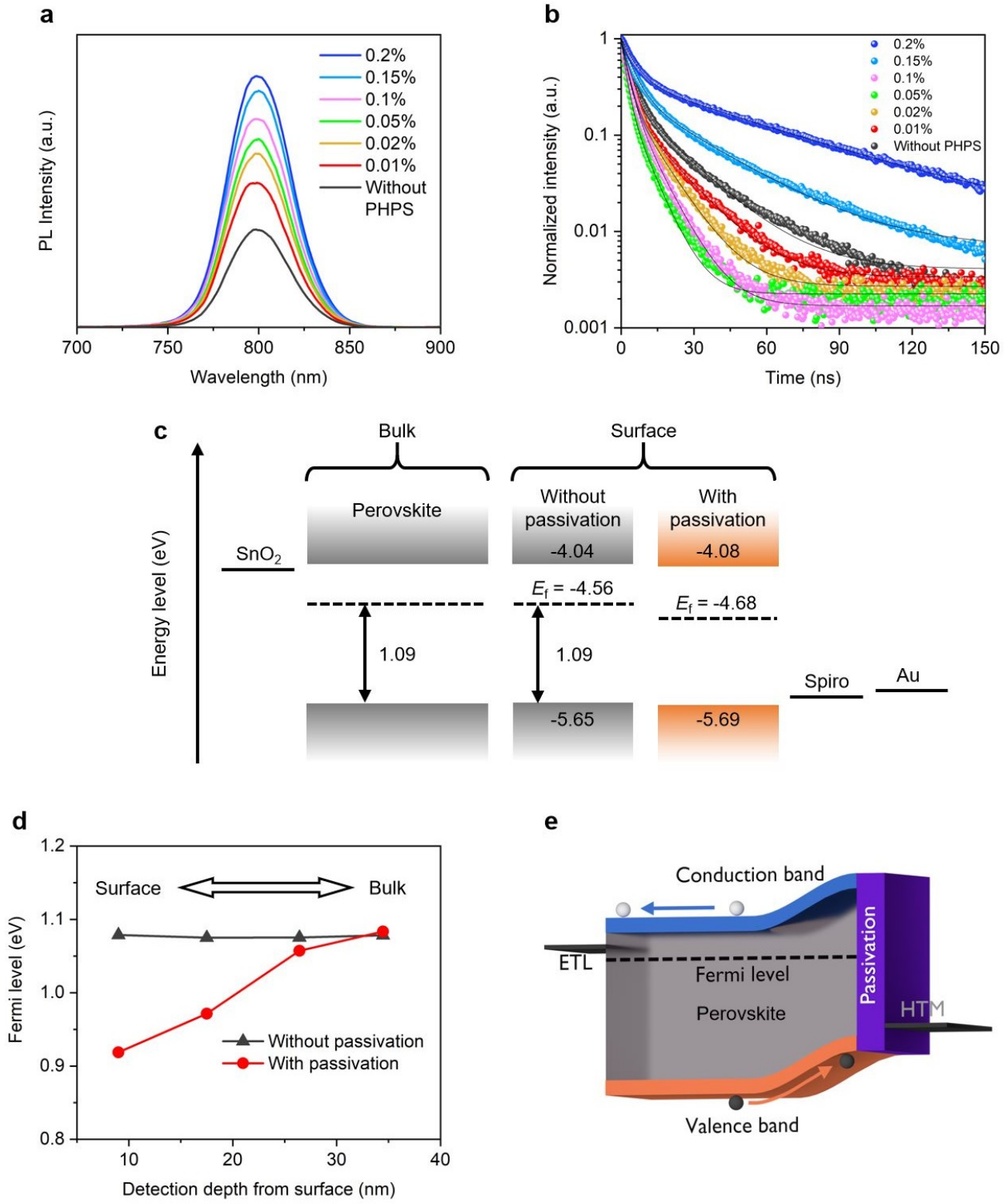

Fig. 5 Effect of perovskite surface passivation with PHPS treatment. a,b, Photoluminescence spectroscopy of steady-state intensity (a) and decay (b) as a function of PHPS solution concentration. **c,** Energy band diagram of the perovskite with and without passivation. **d,**

Fermi level as a function of the detection depth from perovskite surface. E_f was shifted from 0.92 eV at 9 nm to 0.1.08 eV at 34 nm. **e,** Effect of band-bending induced passivation. PHPS concentration is 0.02 vol.% for the energy diagram.

To test how the inorganic passivation layer affected light stability, we measured the continuous performance of perovskite solar cells with and without passivation by maximum power point (MPP) tracking (Fig. 6). After 1000 h, we observed that cells with passivation maintained 77% of the initial efficiency, which was considerably higher than that for the cell without passivation (50% at 1000 h). In addition, devices stored in dry air and measured periodically, the passivated solar cell maintained 99% efficiency after 3900 h (Supplementary Fig. 12). These results indicate that applying inorganic passivation resulted not only in enhanced hole extraction from the bulk to the HTM but also in a more stable perovskite solar cell.

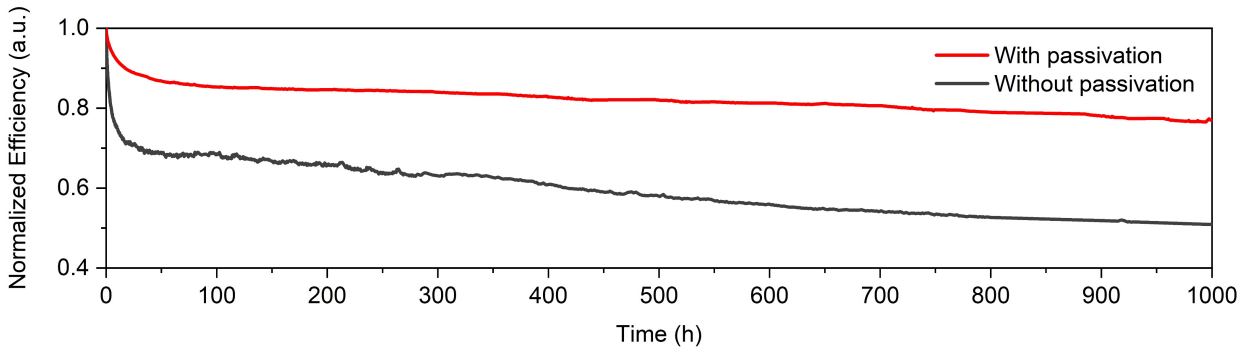

Fig. 6 Light stability of perovskite solar cells with and without passivation. Light stability of perovskite solar cells with and without passivation was measured by maximum power point tracking. PHPS concentration was 0.02 vol.%.

Finally, it was tested whether protection layer using PHPS could also serve as a water repellant protection layer for perovskite solar cells (Fig. **7**). In this experiment, the device structure was changed to FTO/c-TiO_2/mp-TiO_2/c-SnO_2/Perovsktie/Spiro-OMeTAD/Au/Protection layer. After measuring the device efficiency, a thick protection layer (500 nm) was deposited on the perovskite solar cell by spin-coating (3000 rpm, 20 vol.%). Water (15 mL) was then dropped on the devices by spin-coating, and the efficiency of the solar cell was measured. Without the protection layer, dripping water on the device resulted in a 74% efficiency decrease and a marked difference in the solar cell appearance (Fig. 7b). However, the normalized efficiency of devices with protection layer was identical to the initial value (Fig. 7a, Supplementary Table 1). Furthermore, the perovskite layer was not degraded (Fig. 7b), as confirmed by X-ray Diffraction (XRD) measurements (Supplementary Fig. 13). We reasoned, therefore, that the hydrophobic protection layer can also act as a water repellent (Supplementary Fig. 14).

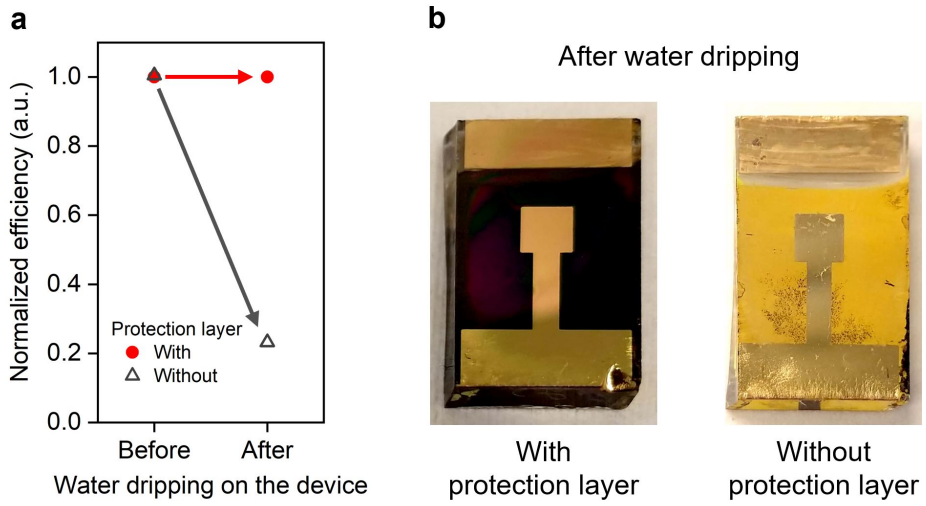

Fig. 7 Perovskite device waterproofing. a, Normalized efficiency before and after water dripping on the device compared with and without protection layer using PHPS. Water was dropped on the device during spin-coating. **b,** Device images after water dripping comparing with and without protection layer. PHPS solution was deposited on the completed device. PHPS concentration is 20 vol.%.

Conclusion

In this manuscript, we have demonstrated that PHPS derived silicon oxide can serve as an effective passivation layer for high-performance perovskite solar cells and elucidated the mechanism of the passivation. It was found that the passivation layer shifts the energy of the Fermi-level of the perovskite surface by improving surface states. Such Fermi-level differences between the perovskite surface and the bulk cause beneficial band-bending at the interface, which acts as a driving force to enhance hole-extraction from the perovskite absorber layer. Consequently, the passivation design strategy we present here can improve the device V_{OC} to >1.1 V and the photoconversion efficiency to 22.13%. As an added benefit, inorganic passivation layer can further improve the device stability compared with the non-treated cells, as well as behaving as remarkable waterproof protection when encapsulating perovskite solar cells.

Methods

Materials

Perhydropolysilazane (PHPS, 20 vol.%) was purchased from AZ Electronic Materials Co., Ltd. O-xylene (99%, extra dry, Across) was purchased from Fisher Sienctific Inc. to dilute the PHPS. For fabrication of perovskite layer, lead iodide and lead bromide were purchased from TCI Co. Ltd. Methylammonium bromide and formamidinium iodide were purchased from GreatCell Solar Ltd. Cesium iodide was obtained from abcr GmbH. All of the purchased chemicals were used as received without further purification. FTO glass (TEC-9AX) was purchased from NSG group. Titanium diisopropoxide bis(acetylacetonate) was purchased from Sigma-Aldrich. Titanium oxide nanoparticle was purchased from PST30NRD from GreatCell Solar. Tin chloride (IV) was purchased Acros Organics. Bis(trifluoromethane)sulfonimide lithium salt and cobalt-complex (FK209) were purchased from Sigma-Aldrich.

Device fabrication

A blocking TiO_2 layer was deposited on cleaned FTO glass by spray pyrolysis deposition of precursor solution (1 mL of titanium diisopropoxide bis(acetylacetonate) in 15 mL ethanol) at 500 °C. Then, mesoporous titanium oxide layer was deposited by spin-coating using a dispersed nanoparticle solution (1 g of in 11.8 g of ethanol) at 5000 rpm for 30 s, followed by annealing at 500 °C for 30 min. Subsequently, the tin-oxide layer was deposited by spin-coating with precursor solution (0.1 M of tin chloride (IV) in deionized water) and annealed at 100 °C for 10 min and 190 °C for 1 h in air.[46] After that, UV/O_3 treatment (PSD series digital UV

ozone system, Novascan Technologies, Inc.) was performed for 15 min. To form the perovskite layer, a perovskite precursor solution was prepared with lead excess $(FAPbI_3)_{0.875}(MAPbBr_3)_{0.125}(CsPbI_3)_{0.1}$ by mixing lead iodide (1.2 M), lead bromide (0.15 M), formamidinium iodide (1.0 M), methylammonium bromide (0.15 M), and cesium iodide (0.13 M) in DMF:DMSO=4:1 (volume ratio). The perovskite solution was spun on the substrate with two-step spin-coating program set as 2000 and 5000 rpm for 10 and 30 s, respectively. During spin-coating, 100 μL of chlorobenzene was dripped on the substrate before 10 s from termination time of the spin-coating. Then, the substrate was annealed at 100 °C for 1 h to crystallize the perovskite layer. After that, solution of PHPS diluted in o-xylene (0.01－0.2 vol.%) was spun-on the substrate at 4000 rpm for 30 s followed by keeping in dry air (5% relative humidity) for 30 min. To deposit hole-transport material (HTM), 80 mg of Spiro-OMeTAD solution was diluted in 1023 μL of chlorobenzene, followed by adding 32 μL of 4-tert-butylpyridine, 19 μL of Bis(trifluoromethane)sulfonimide lithium salt solution (517 mg mL^{-1}) in acetonitrile, and 14 μL of cobalt-complex solution (376 mg mL^{-1}) in acetonitrile. The prepared Spiro-OMeTAD solution was spun-on the substrate at 4000 rpm for 30 s. At last, 70 nm of Au layer was deposited on the HTM as a counter electrode.

Characterizations and measurements

I-V was measured by using an Oriel VeraSol solar simulator (Newport Corporation) calibrated by LCE-50 (Centronics). The *I-V* measurement was performed from 1.2 to 0 V as a reverse scan and from 0 to 1.2 V as forward scan with a mask of 3×3 mm^2. Scanning step and speed was 10 mV and 50 mV/s, respectively. UV/VIS

spectroscopy was measured using a Lambda 950S (PerkinElmer, Inc.). Photoluminescence emission spectra were measured using LS-55 fluorescence spectrometer (PerkinElmer, Inc.). Time-resolved photoluminescence was measured by a time-correlated single photon counting system (Nanofinder 30.). The wavelength for excitation was 480 nm. The wavelength for the detector was 791－797 nm. Morphology was assessed by a cold field emission scanning electron microscope (SU8200, Hitachi high-tech. Co.) One dimensional X-ray diffraction (XRD) analysis was carried out using a D8 Advance diffractometer (Bruker Corporation) with Cu Kα radiation ($\lambda_{K\alpha}$ = 1.5418 Å). Two-dimensional Wide-Angle X-ray Scattering (2D-WAXS) patterns represented in reciprocal lattice space were conducted at Spring-8 on beamline BL19B2. The sample was irradiated with X-ray energy of 12.39 keV (λ = 1 Å) at a fixed incident angle on the order of 6.0° through a Huber diffractometer. The 2D-WAXS patterns were recorded with a two-dimensional image detector (Pilatus 300K). UPS equipped with He-I source (hν = 21.22 eV) (AXIS Nova, Kratos Analytical Ltd., UK) was used to determine the valence band energy and Fermi level. The Fermi level of the samples was referred to that of Au which was in electrical contact with a sample in UPS measurements. Angle-Resolved Hard X-ray Photoemission Spectroscopy (AR-HAXPES) at 8000eV was measured by the system of Scienta R4000 with BL46XU beamline in Spring-8. The XPS measurements were carried out on a VersaProbe II (Physical Electronics Inc) with a monochromator and source of Al-Kα 1486.6KeV. The spectrum was referenced using the C-C bound component of the adventitious carbon. The stability test was measured as maximum power tracking under 100 mW cm^{-2} illumination with LED power source encapsulating samples into the measurement box purging argon gas with 0% of humidity kept at 25 °C by the cooling system.

Stereo image

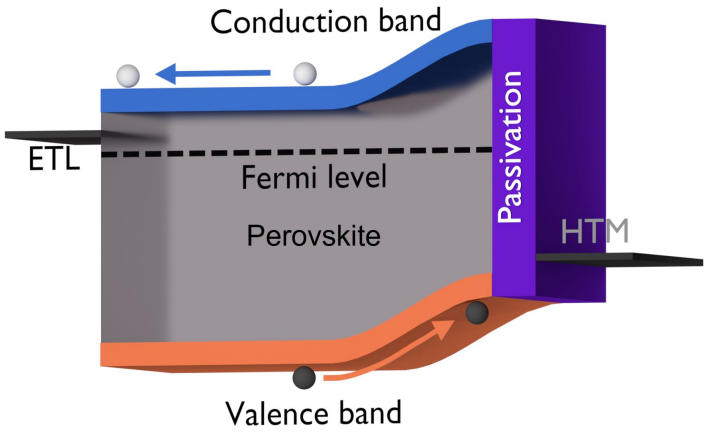

Acknowledgments

The authors acknowledge financial support from CTI 25590.1 PFNM-NM, Solaronix, Aubonne, Switzerland, Toyota Motor Corporation, Toyota Motor Technical Centre, Advanced Technology Div., Hoge Wei 33, B-1930 Zaventum, Belgium, and US Army grant agreement No. W911NF-17-2-0122. We thank Dr. N. Valle, Dr. P. Gratia, Dr. B. E. Adib, and Dr. J-N. Audinoz in Luxembourg Institute of Science and Technology for device characterization; Dr. S. Yasuno, and Dr. T. Koganezawa in Japan Synchrotron Radiation Research Institute (JASRI) and Y. Nakamura in Univ. Tokyo for discussions. The 2D-WAXS measurement was performed at SPring-8 at BL19B2 with the approval of the JASRI, proposal nos. 2018B1809, 2018B1855 and 2018B1862. The X-ray Photoelectron Spectroscopy Measurement SPring-8 at BL46XU with the approval of the JASRI, proposal nos. 2018B1868 and 2019A1719. M. Li would like to thank the China Scholarship Council for the Ph.D. grant (Grant No. 201506060156).

Contributions

H.K. conceived the idea, device fabrication and wrote the manuscript. N.S assist in writing the manuscript and performed SEM, 2D-WAXS, PL decay, UPS, and AR-HAXPES experiments and analyzed the data. A.J.H., Y.L., S.P., N.K., C.R., V.L.E.Q., G.G., Y.Z., M.A., and K.T.C. assist in device fabrication. M.D.M. and M.L. assist in XPS measurement. M.K.N supervised the project. All authors contributed to discussions and to finalizing the manuscript.

Reference

1. Kojima, A., Teshima, K., Shirai, Y. & Miyasaka, T. Organometal halide perovskites as visible-light sensitizers for photovoltaic cells. *J. Am. Chem. Soc.* **131**, 6050–6051 (2009).

2. Kim, H.-S. et al. Lead iodide perovskite sensitized all-solid-state submicron thin film mesoscopic solar cell with efficiency exceeding 9%. *Sci. Rep.* **2**, 591 (2012).

3. Lee, M. M., Teuscher, J., Miyasaka, T., Murakami, T. N. & Snaith, H. J. Efficient hybrid solar cells based on meso-superstructured organometal halide perovskites. *Science* **338**, 643–647 (2012).

4. Im, J.-H., Lee, C.-R., Lee, J.-W., Park, S.-W. & Park, N.-G. 6.5% efficient perovskite quantum-dot-sensitized solar cell. *Nanoscale* **3**, 4088 (2011).

5. Jeon, N. J. et al. Compositional engineering of perovskite materials for high-performance solar cells. *Nature* **517**, 476–480 (2015).

6. Jeon, N. J. et al. A fluorene-terminated hole-transporting material for highly efficient and stable perovskite solar cells. *Nat. Energy* **3**, 682–689 (2018).

7. Jiang, Q. et al. Enhanced electron extraction using SnO_2 for high-efficiency planar-structure $HC(NH_2)_2PbI_3$-based perovskite solar cells. *Nat. Energy* **2**, 16177 (2017).

8. Wei, M. et al. Ultrafast narrowband exciton routing within layered perovskite nanoplatelets enables low-loss luminescent solar concentrators. *Nat. Energy* **4**, 197–205 (2019).

9. Zhou, H. et al. Interface engineering of highly efficient perovskite solar cells. *Science* **345**, 542–546 (2014).

10. Best Research-Cell Efficiencies (NREL, 2019). Available at: https://www.nrel.gov/pv/cell-efficiency.html.

11. Chen, Z. et al. Thin single crystal perovskite solar cells to harvest below-bandgap light absorption. *Nat. Commun.* **8**, 1890 (2017).

12. Lin, Q., Armin, A., Nagiri, R. C. R., Burn, P. L. & Meredith, P. Electro-optics of perovskite solar cells. *Nat. Photonics* **9**, 106–112 (2015).

13. Wehrenfennig, C., Eperon, G. E., Johnston, M. B., Snaith, H. J. & Herz, L. M. High Charge Carrier Mobilities and Lifetimes in Organolead Trihalide Perovskites. *Adv. Mater.* **26**, 1584–1589 (2014).

14. Xing, G. et al. Long-range balanced electron-and hole-transport lengths in organic-inorganic $CH_3NH_3PbI_3$. *Science* **342**, 344–347 (2013).

15. Mei, A. et al. Electron-hole diffusion lengths > 175 μm in solution-grown $CH_3NH_3PbI_3$ single crystals. *Science* **347**, 967–970 (2015).

16. Stranks, S. D. et al. Electron-hole diffusion lengths exceeding 1 micrometer in an organometal trihalide perovskite absorber. *Science* **342**, 341–344 (2013).

17. Eperon, G. E. et al. Formamidinium lead trihalide: a broadly tunable perovskite for efficient planar heterojunction solar cells. *Energy Environ. Sci.* **7**, 982 (2014).

18. Xing, G. et al. Low-temperature solution-processed wavelength-tunable perovskites for lasing. *Nat. Mater.* **13**, 476–480 (2014).

19. Huang, H. et al. Growth mechanism of strongly emitting $CH_3NH_3PbBr_3$ perovskite nanocrystals with a

tunable bandgap. *Nat. Commun.* **8**, 996 (2017).

20. Polman, A., Knight, M., Garnett, E. C., Ehrler, B. & Sinke, W. C. Photovoltaic materials: Present efficiencies and future challenges. *Science* **352**, aad4424 (2016).

21. Tress, W. Perovskite Solar Cells on the Way to Their Radiative Efficiency Limit – Insights Into a Success Story of High Open-Circuit Voltage and Low Recombination. *Adv. Energy Mater.* **7**, 1602358 (2017).

22. Shockley, W. & Queisser, H. J. Detailed balance limit of efficiency of p-n junction solar cells. *J. Appl. Phys.* **32**, 510–519 (1961).

23. Bi, D. et al. Polymer-templated nucleation and crystal growth of perovskite films for solar cells with efficiency greater than 21%. *Nat. Energy* **1**, 16142 (2016).

24. Zuo, L. et al. Polymer-modified halide perovskite films for efficient and stable planar heterojunction solar cells. *Sci. Adv.* **3**, e1700106 (2017).

25. Chaudhary, B. et al. Poly(4-Vinylpyridine)-Based Interfacial Passivation to Enhance Voltage and Moisture Stability of Lead Halide Perovskite Solar Cells. *ChemSusChem* **10**, 2473–2479 (2017).

26. Jiang, Q. et al. Surface passivation of perovskite film for efficient solar cells. *Nat. Photonics* **1** (2019). doi:10.1038/s41566-019-0398-2

27. Jung, E. H. et al. Efficient, stable and scalable perovskite solar cells using poly(3-hexylthiophene). *Nature* **567**, 511–515 (2019).

28. Zheng, X. et al. Defect passivation in hybrid perovskite solar cells using quaternary ammonium halide anions and cations. *Nat. Energy* **2**, 17102 (2017).

29. Noel, N. K. et al. Highly Crystalline Methylammonium Lead Tribromide Perovskite Films for Efficient Photovoltaic Devices. *ACS Energy Lett.* **3**, 1233–1240 (2018).

30. Tan, H. et al. Efficient and stable solution-processed planar perovskite solar cells via contact passivation. *Science* **355**, 722–726 (2017).

31. Zhang, Z. & Yates, J. T. Band Bending in Semiconductors: Chemical and Physical Consequences at Surfaces and Interfaces. *Chem. Rev.* **112**, 5520–5551 (2012).

32. Mallorquí, A. D. et al. Field-effect passivation on silicon nanowire solar cells. *Nano Res.* **8**, 673–681 (2015).

33. Mews, M., Liebhaber, M., Rech, B. & Korte, L. Valence band alignment and hole transport in amorphous/crystalline silicon heterojunction solar cells. *Appl. Phys. Lett.* **107**, 013902 (2015).

34. Çopuroğlu, M., Sezen, H., Opila, R. L. & Suzer, S. Band-Bending at Buried SiO_2/Si Interface as Probed by XPS. *ACS Appl. Mater. Interfaces* **5**, 5875–5881 (2013).

35. Varache, R., Kleider, J. P., Favre, W. & Korte, L. Band bending and determination of band offsets in amorphous/crystalline silicon heterostructures from planar conductance measurements. *J. Appl. Phys.* **112**, 123717 (2012).

36. Sun, Y. N., Feldman, A. & Farabaugh, E. N. X-ray photoelectron spectroscopy of O 1s and Si 2p lines in films of SiOx formed by electron beam evaporation. *Thin Solid Films* **157**, 351–360 (1988).

37. Naskar, S., Wolter, S. D., Bower, C. A., Stoner, B. R. & Glass, J. T. Verification of the O–Si–N complex in plasma-enhanced chemical vapor deposition silicon oxynitride films. *Appl. Phys. Lett.* **87**, 261907

(2005).

38. Saliba, M. et al. Cesium-containing triple cation perovskite solar cells: improved stability, reproducibility and high efficiency. *Energy Environ. Sci.* **9**, 1989–1997 (2016).

39. Xie, L.-Q. et al. Understanding the Cubic Phase Stabilization and Crystallization Kinetics in Mixed Cations and Halides Perovskite Single Crystals. *J. Am. Chem. Soc.* **139**, 3320–3323 (2017).

40. Tsai, H. et al. Light-induced lattice expansion leads to high-efficiency perovskite solar cells. *Science* **360**, 67–70 (2018).

41. Wolff, C. M. et al. Reduced Interface-Mediated Recombination for High Open-Circuit Voltages in $CH_3NH_3PbI_3$ Solar Cells. *Adv. Mater.* **29**, 1700159 (2017).

42. Shibayama, N., Kanda, H., Kim, T. W., Segawa, H. & Ito, S. Design of BCP buffer layer for inverted perovskite solar cells using ideal factor. *APL Mater.* **7**, 031117 (2019).

43. Tanuma, S., Powell, C. J. & Penn, D. R. Calculations of electron inelastic mean free paths. V. Data for 14 organic compounds over the 50-2000 eV range. *Surf. Interface Anal.* **21**, 165–176 (1994).

44. Philippe, B. et al. Valence Level Character in a Mixed Perovskite Material and Determination of the Valence Band Maximum from Photoelectron Spectroscopy: Variation with Photon Energy. *J. Phys. Chem. C* **121**, 26655–26666 (2017).

45. Philippe, B. et al. Chemical Distribution of Multiple Cation (Rb^+, Cs^+, MA^+, and FA^+) Perovskite Materials by Photoelectron Spectroscopy. *Chem. Mater.* **29**, 3589–3596 (2017).

46. Lee, Y. et al. Enhanced charge collection with passivation of the tin oxide layer in planar perovskite solar

cells. *J. Mater. Chem. A* **5**, 12729–12734 (2017).